Journal of Power Sources 328 (2016) 203–211

Contents lists available at ScienceDirect

Journal of Power Sources

journal homepage: www.elsevier.com/locate/jpowsour

Computational design and refinement of self-heating lithium ion batteries

Xiao-Guang Yang, Guangsheng Zhang, Chao-Yang Wang*

Department of Mechanical and Nuclear Engineering and Electrochemical Engine Center (ECEC), The Pennsylvania State University, University Park, PA 16802, USA

HIGHLIGHTS

- We present & validate the first model for a new class of self-heating Li-ion batteries.
- Non-uniform temperature and current distributions in a SHLB are predicted.
- Internal temperature gradient greatly affects self-heating time & energy consumption.
- Multi-sheet design with optimized self-heating time & energy consumption is proposed.

GRAPHICAL ABSTRACT

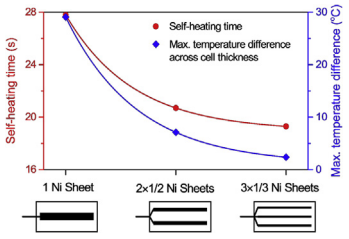

ARTICLE INFO

Article history:
Received 11 June 2016
Received in revised form
23 July 2016
Accepted 5 August 2016

Keywords:
Lithium ion battery
Self-heating
Temperature gradient
Numerical modeling
Low temperature performance

ABSTRACT

The recently discovered self-heating lithium ion battery has shown rapid self-heating from subzero temperatures and superior power thereafter, delivering a practical solution to poor battery performance at low temperatures. Here, we describe and validate an electrochemical-thermal coupled model developed specifically for computational design and improvement of the self-heating Li-ion battery (SHLB) where nickel foils are embedded in its structure. Predicting internal cell characteristics, such as current, temperature and Li-concentration distributions, the model is used to discover key design factors affecting the time and energy needed for self-heating and to explore advanced cell designs with the highest self-heating efficiency. It is found that ohmic heat generated in the nickel foil accounts for the majority of internal heat generation, resulting in a large internal temperature gradient from the nickel foil toward the outer cell surface. The large through-plane temperature gradient leads to highly non-uniform current distribution, and more importantly, is found to be the decisive factor affecting the heating time and energy consumption. A multi-sheet cell design is thus proposed and demonstrated to substantially minimize the temperature gradient, achieving 30% more rapid self-heating with 27% less energy consumption than those reported in the literature.

1. Introduction

Lithium ion batteries suffer from severe performance loss at low temperatures [1–4], limiting their use in many applications like electric vehicles (EVs). The driving range of EV per charge, 105 miles at 75 °F (23.9 °C) as reported by American Automobile Association [5], drops by 57% to 43 miles at 20 °F (−6.7 °C), exacerbating driving range anxiety which is already a major barrier to mainstream adoption of EVs. Fundamental reasons for poor battery performance at low temperatures include high viscosity of the electrolyte

* Corresponding author.
E-mail address: cxw31@psu.edu (C.-Y. Wang).

http://dx.doi.org/10.1016/j.jpowsour.2016.08.028
0378-7753/

and hence low Li^+ diffusivity, low ionic conductivity of the electrolyte, high solid-electrolyte interphase (SEI) layer impedance, and high interfacial kinetic resistances, especially in the graphite anode.

Much work has been conducted in the past decade to improve the performance of Li-ion batteries at subzero temperatures [6–12]. One prevalent approach is to search for additives that can improve electrolyte performance at low temperatures [10,13]. Most of these electrolyte additives, however, also deteriorate cell performance and cycle life at high temperatures. Another approach is to preheat the battery to an optimal temperature before use [14–16]. Ji and Wang [16] thoroughly reviewed a wide range of heating strategies, although most have such issues as low heating efficiency, long heating time and high energy consumption.

Most recently, we experimentally discovered a novel battery structure, the self-heating Li-ion battery (SHLB) [3], which can rapidly self-heat from −30 °C to 0 °C in less than 30 s and thereafter bring about a 10-fold power boost over state-of-art Li-ion batteries, with only ~5.5% of cell energy consumed. Fig. 1a illustrates the structure of an SHLB. Aside from the three main components of a conventional Li-ion cell: an anode, a cathode and an electrolyte/separator, the SHLB inserts a thin nickel (Ni) foil, coated with electrically insulating polymer and sandwiched between two single-sided anode layers, into the center of the SHLB. One end of the Ni foil is connected to the negative terminal, welded together with tabs of all anode layers. The other end of the Ni foil extends outside the cell to form a third terminal, the activation terminal. A switch is used to connect the activation terminal with the negative terminal. The working principle of the SHLB can be explained via the electrical circuit diagram in Fig. 1b. At temperatures lower than 0 °C, the switch is left open to force current flow through the Ni foil, generating substantial ohmic heat that rapidly warms up the battery materials and electrochemical interfaces. Once the cell temperature reaches or exceeds 0 °C, the switch is closed such that the current bypasses the Ni foil and the cell acts as a conventional cell, working in the optimal temperature range with superior performance.

Here, for the first time, we describe an electrochemical-thermal (ECT) coupled model developed to seek a fundamental understanding of the self-heating process (hereafter referred to as activation) and to discover key design factors affecting the time and energy needed for self-heating. Furthermore, we shall unravel a major advance in the SHLB technology through computer simulations.

2. Electrochemical-thermal coupled model

The SHLB pouch cell contains a number of multiple anode and cathode layers with separators in between, along with a thin nickel foil for self-heating stacked in the middle of the cell, as illustrated in Fig. 1a. Each anode or cathode layer is composed of a current-collecting foil with active materials coated on both sides. Given the stacking structure, the pouch cell can be considered as multiple cell units connected in parallel, each composed of one anode layer, one cathode layer, and two separators, as illustrated in Fig. 1a. Fig. S1 in the electronic supplementary information (ESI) depicts the current flow among the various cell units as well as the Ni foil in the activation process of the SHLB. All cell units share the same voltage, but we shall note that the current of each unit may be quite different if their local states such as temperature and state of charge (SOC), differ.

A generic electrochemical-thermal (ECT) modeling framework based on three-grid method of Luo and Wang [17] and Kalupson et al. [18] is adopted here. In it the thermal model is solved on a macro-scale grid discretizing a multi-layer, large-format cell (displayed in Fig. 1c, where each mesh corresponds to one cell unit defined in Fig. 1a). Each cell unit is further discretized into a set of meso-grids in the thickness direction (Fig. 1d), on which the electrochemical processes are simulated. In addition, the solid-state diffusion is numerically solved on the micro-grid dividing active material particles into a number of finite elements (Fig. 1d). These model components are briefly summarized in the following.

2.1. Electrochemical model

The electrochemical model for each cell unit of anode/electrolyte-separator/cathode contains the following conservation equations:

Charge conservation in solid electrodes:

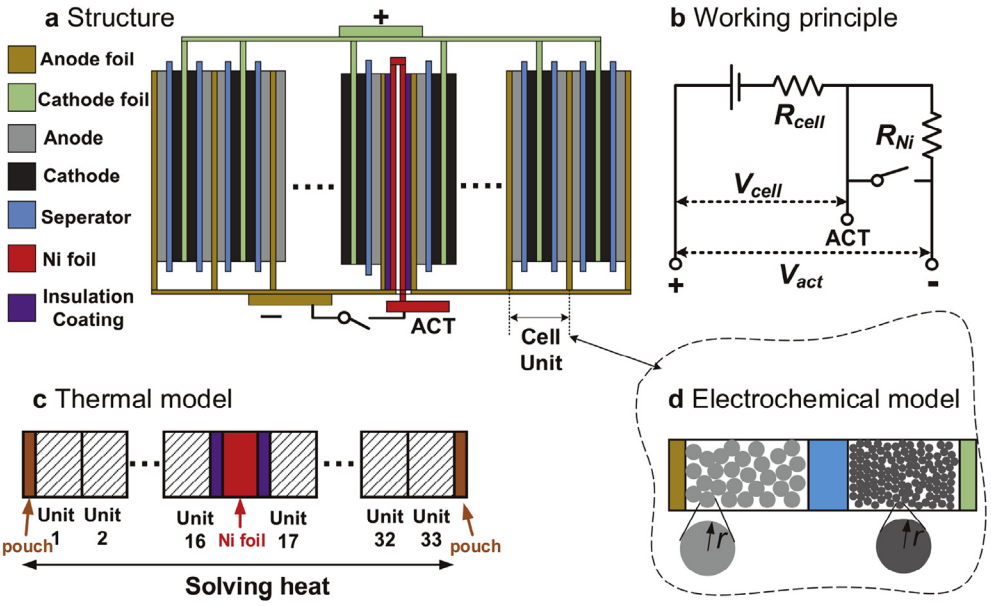

Fig. 1. (a) Structure of a self-heating Li-ion battery (SHLB) and illustration of the multi-layer pouch cell. (b) Electrical circuit diagram showing the working principle of the SHLB and definition of cell voltage (V_{cell}) and activation voltage (V_{act}). (c) Sketch of the thermal model. (d) Sketch of the electrochemical model corresponding to one cell unit.

$$\nabla\cdot\left(\sigma_s^{eff}\nabla\phi_s\right)=j \tag{1}$$

Charge conservation in electrolyte:

$$\nabla\cdot\left(\kappa^{eff}\nabla\phi_e\right)+\nabla\cdot\left(\kappa_D^{eff}\nabla\ln c_e\right)=-j \tag{2}$$

Species conservation in electrolyte:

$$\frac{\partial(\varepsilon c_e)}{\partial t}=\nabla\cdot\left(D^{eff}\nabla c_e\right)+\frac{1-t_+}{F}j \tag{3}$$

Species conservation in active material particles:

$$\frac{\partial c_s}{\partial t}=\frac{1}{r^2}\frac{\partial}{\partial r}\left(D_s r^2\frac{\partial c_s}{\partial r}\right) \tag{4}$$

Detailed explanations for the above equations were presented in the literature [4,19] and therefore are not repeated here. Equations (1)–(3) are solved on the meso-grid, while Equation (4) is solved numerically on the micro-grid. Most parameters in these equations, such as lithium diffusivity in electrolyte and in active materials, exchange current density for anode and cathode reactions, etc., depend highly on temperature of the corresponding cell unit, which is obtained by solving the thermal model presented in Section 2.2. Boundary conditions for these equations along with details of their numerical implementation can be found in Ref. [4]. Parameters related to the above equations, such as the properties of the graphite anode and the electrolyte, are taken either from the material database of Autolion™ [20], a commercial software package for analyses of electrochemical and thermal interactions of Li-ion batteries and systems, or from Ref. [4]. The properties of cathode materials, the $LiNi_{0.6}Co_{0.2}Mn_{0.2}O_2$, including the open-circuit potential, solid-state diffusivity and exchange current density, over a range of temperatures from −30 to 60 °C and electrolyte concentration from 0 to 4 M, are obtained from the experiments of Leng and Wang [21].

2.2. Thermal model

The governing equation for thermal energy conservation can be expressed as:

$$\frac{\partial(\rho c_p T)}{\partial t}=\nabla\cdot(\kappa\nabla T)+q \tag{5}$$

where ρ, c_p, κ and T are density, heat capacity, thermal conductivity and temperature. The thermal properties used in this work are summarized in Table 1. Note that the properties of cell unit are averaged values of the components constituting the units (i.e. Cu and Al foils, anode, cathode and separator), using algorithms detailed in Ye et al. [22].

The term q in Equation (5) represents the heat generation rate. During activation, heat is generated both within the Ni foil and in each cell unit. The heat source in the Ni foil is calculated as:

$$q_{\mathrm{Ni}}=\frac{I_{tot}^2\cdot R_{Ni}}{V_{Ni}} \tag{6}$$

where I_{tot}, R_{Ni} and V_{Ni} are total cell current, Ni foil resistance and Ni foil volume. It should be noted that the Ni foil resistance depends strongly on temperature, as shown in Fig. S2 of ESI, and can be correlated as

$$R_{Ni}=R_{Ni,ref}\left(1+\alpha\left(T-T_{ref}\right)\right) \tag{7}$$

where $R_{Ni,ref}$ is the reference resistance measured at the reference temperature T_{ref}, and α is the temperature coefficient. For the present work, $R_{Ni,ref}$, T_{ref}, and α are equal to 56.2 mΩ, 20 °C and 0.00517 K^{-1}, respectively.

The heat source in each cell unit is calculated by:

$$q_{Unit}=j\left(T\frac{\partial U}{\partial T}\right)+j(\phi_s-\phi_e-U)+\sigma_s^{eff}\nabla\phi_s\cdot\nabla\phi_s+\kappa^{eff}\nabla\phi_e\cdot\nabla\phi_e+\kappa_D^{eff}\nabla\ln c_e\cdot\nabla\phi_e \tag{8}$$

where the first and second terms on the right-hand-side (RHS) represent reversible heat and kinetic heat of the cell unit; the third, fourth and fifth terms on the RHS of Equation (8) are the ohmic heat due to electronic resistance, ionic resistance and electrolyte concentration overpotential respectively. All these terms are calculated based on the electrochemical model. The electrochemical and thermal models are fully coupled through temperature-dependent electrochemical and physical properties as well as the heat generation expression in Eqs. (6) and (8).

3. Experimental

Experiments are carried out to obtain data for validation of the present ECT model. These results include temperatures of the cell surface and the Ni foil, as well as the current and voltage of the SHLB cell in the activation process. In this work, we denote the voltage between the positive and negative terminals (referring to Fig. 1b) as the cell voltage, V_{cell}, and the voltage between the positive and activation terminals as activation voltage, V_{act}. In accordance with our previous work [3], the activation of the SHLB is implemented by setting the activation voltage to a constant value, i.e. 0.4 V.

Table 1
Thermal properties of battery materials and cell units.

	Thickness (μm)	Density (kg m^{-3})	Specific heat (J kg^{-1} K^{-1})	Thermal conductivity (W m^{-1} K^{-1})
Cu foil	10	8900	385	398
Anode	48.7	1347.3	1473.4	1.04
Separator	25	1008.9	1978.2	0.3344
Cathode	40.75	1500	1260.2	1.48
Al foil	15	2700	903	238
Electrolyte	N/A	1129.95	2055.1	0.6
Cell unit	253.9	1707.1	1195.2	0.55
Ni foil	50	8900	444	90.9
Insulation coating	28	1380	1000	0.2
Cell pouch	100	1920	946	2.0

3.1. Experimental cell

We fabricate a 10 Ah SHLB pouch cell with $LiNi_{0.6}Co_{0.2}Mn_{0.2}O_2$ as the cathode, graphite as the anode and 1 M of $LiPF_6$ dissolved in EC/EMC (3:7 by wt.) + 2 wt% VC as electrolyte. The capacity ratio between negative and positive electrodes, or N-P ratio, is designed at 1.2. A Celgard-2325 separator of 25 μm in thickness is used. The cell contains a stack of 34 anode and 33 cathode layers, with the top and bottom anode layers single-side coated. Therefore it corresponds to a total of 33 individual cell units given the definition illustrated in Fig. 1a. A Ni foil of 50 μm in thickness and 56.2 mΩ in resistance at 20 °C is coated with a thin (28 μm) backing material of polyethylene terephthalate on both sides for electrical insulation, and sandwiched between 2 single-sided anode layers. This 3-layer assembly is then stacked in the center of the cell (i.e. between the 16th and 17th cell units). Other details of the SHLB cell, such as the compositions of electrodes, are the same as in our previous work [3].

3.2. Activation protocol

Prior to each activation test, the cell is soaked in an environmental chamber for 8–12 h to reach thermal equilibrium with the subfreezing ambient. Then constant voltage activation is applied to the cell by setting V_{act} at 0.4 V. A battery tester (BT2000, Arbin Instruments, USA) is used to control the activation voltage of the experimental cell, and also to monitor the cell voltage and overall activation current. A temperature-controlled switch is used to connect the negative and activation terminals, which is open throughout the activation process, and is closed once the cell surface temperature reaches 0 °C, or a preset threshold temperature for switching. Then the electrical load is removed to let the cell rest in open-circuit.

3.3. Measurement of cell outer surface and Ni foil temperatures

As shown in Fig. S2, the resistance of Ni foil varies perfectly linearly with the temperature. Thus, the Ni foil can serve as both a heating element and a resistance temperature detector (RTD) to measure the internal cell temperature. In the experiments, both cell voltage and activation voltage are simultaneously monitored during activation, permitting to determine the Ni foil resistance in-situ through dividing the voltage drop (V_{cell}-V_{act}) by the total activation current. The resistance can then be converted into Ni foil temperature using the calibrated resistance-temperature curve (Equation (7)). In addition, the outer surface temperature of the cell is measured by a T-type thermocouple.

4. Results & discussion

4.1. Model validation

Fig. 2a compares the numerical results with the experiment data of the cell surface and Ni foil temperatures during activation. Unless otherwise indicated, all the activation process presented in this work refers to surface temperature rise from −20 to 0 °C. We can see from Fig. 2a that the temperature of internal Ni foil increases much faster than the surface temperature, reaching ~30 °C at the end of activation when the surface temperature rises to 0 °C. This large temperature gradient within the cell is expected to result in great differences in characteristics of different cell units, as will be detailed in the next subsection. It can be noted from Fig. 2a that the predicted surface and Ni foil temperatures match well with the measurements. The simulated total activation current (sum of current of all cell units) and cell voltage also agree well with the experiment data, as shown in Fig. 2b.

4.2. Impact of temperature gradient on cell characteristics

Fig. 3a shows the predicted temperature distribution across the cell thickness at different time instants of activation. Local current generated by different cell units is given in Fig. 3b, which is plotted as a dimensionless C-rate with the 1C current equal to the designed capacity of each unit. The center region near the Ni foil is heated up rapidly upon activation (Fig. 3a). Benefited from the rapid warmup, cell units near the Ni foil produce much higher current, reaching over 9C after 10 s. Cell units near the outer surface, however, discharge at lower than 5C and the current in these units even decreases with time, as can be seen from Fig. 3b.

The large temperature gradient inside the cell is mainly due to insufficient heat transfer in the through-plane direction from the Ni foil to the outer cell surfaces. Most heat in the activation process is generated via ohmic heating in the Ni foil, as can be seen from Fig. 4a. The fraction of heat generated by Ni foil over the total internal heat generation, also plotted in Fig. 4a, ranges from 63% of the overall heat generation at the beginning of activation to 87% at the end, with the average of 78% over the entire activation.

To better illustrate the different characteristics of individual cell units during activation, we select several cell units at different

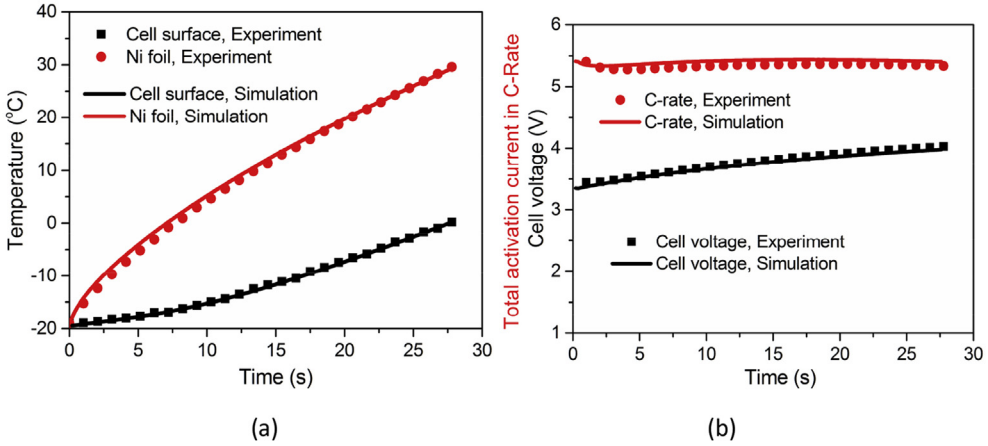

Fig. 2. Experimental (symbols) and numerical (lines) results for (a) temperatures of cell surface and Ni foil and (b) cell voltage and total activation current (in C-rate based on nominal capacity of 10 A h) in the V_{act} = 0.4 V activation process from ambient temperature of −20 °C.

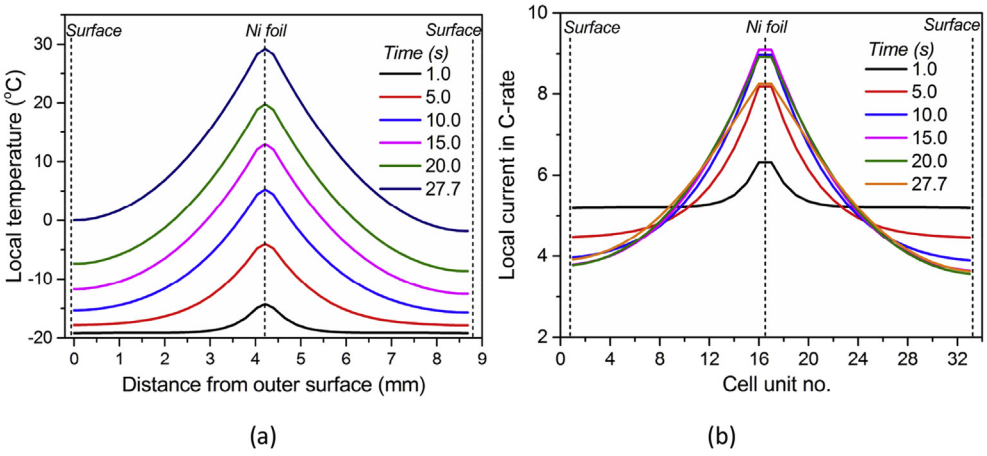

Fig. 3. Distributions of (a) local temperature across cell thickness and (b) local current in C-rate of individual cell units in the V_{act} = 0.4 V activation process from the ambient temperature of −20 °C.

locations of the pouch cell and plot in Fig. 4b and c the evolution of their local temperature and current (in C-rate). Unit 1 is closest to the outer surface and unit 16 is immediately adjacent to the Ni foil. In the closest vicinity of the Ni foil, the temperature of unit 16 increases from −20 to −5.0 °C in only 5 s, as shown in Fig. 4b. Benefited from the rapid temperature rise, the discharge current of unit 16 increases to 8.2 C in 5 s, as shown in Fig. 4c. The temperature of unit 1, however, increases much slower (to −17.8 °C in 5 s and −15.3 °C in 10 s). It is also interesting to note that the discharge current of cell unit 1 even decreases with time in the activation process.

The current of each cell unit can be estimated by $(U_{oc,i} - V_{cell})/R_i$, with $U_{oc,i}$ and R_i denoting the open-circuit voltage and internal resistance of that unit. In the activation process, the open-circuit

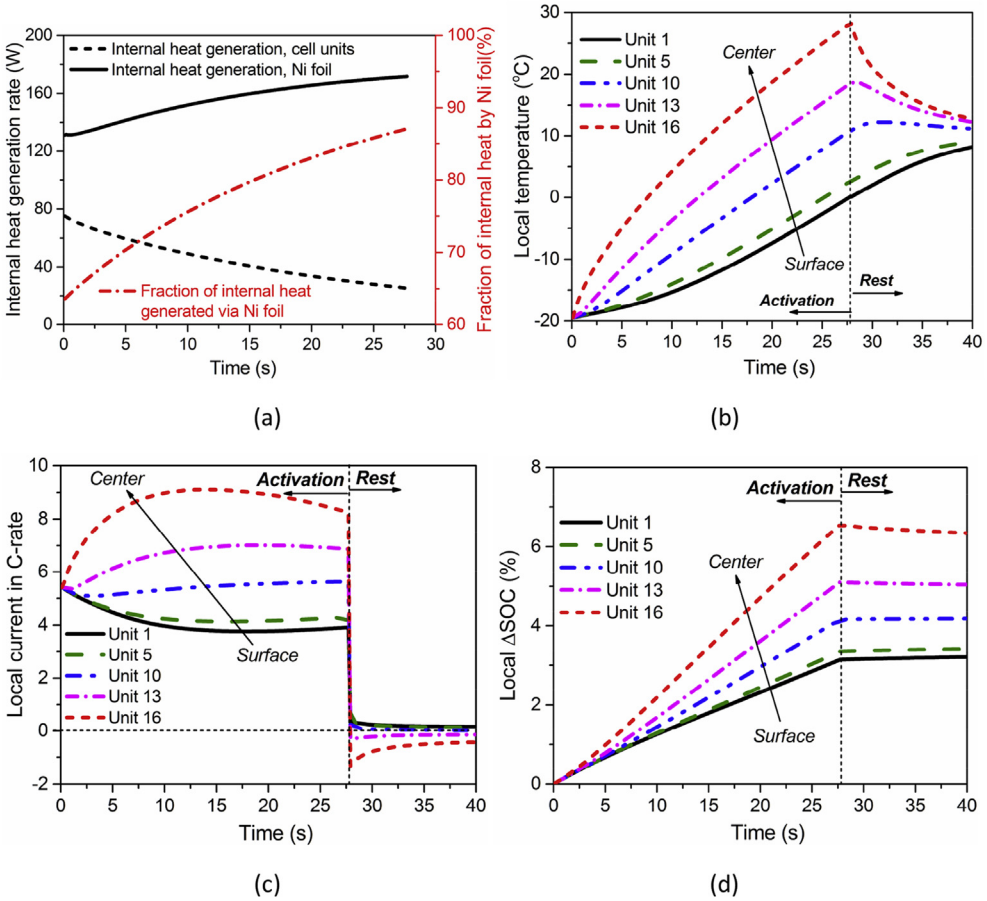

Fig. 4. (a) Variation of heat generation rate in nickel (Ni) foil and in all cell units, and the fraction of heat generated in the Ni foil (ratio between heat generation in Ni foil and total heat generation) in the activation process. (b)~(d): Variation of (b) local temperature, (c) local current in C-rate and (d) local change in state of charge (SOC) during the activation process for several selected cell units at different locations of the self-heating lithium ion pouch cell. Unit 1 is close to cell surface and unit 16 is adjacent to Ni foil.

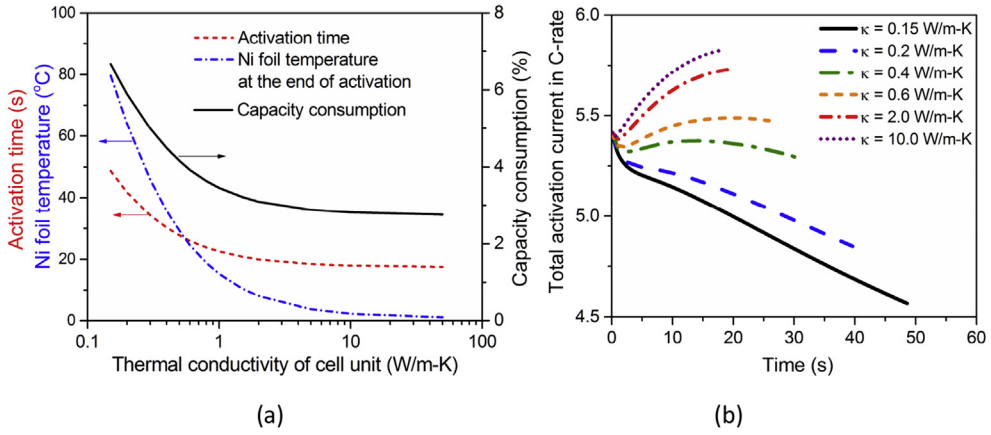

Fig. 5. Simulation results of (a) activation time, nickel (Ni) foil temperature at the end of activation, and capacity consumption for cases with different effective thermal conductivity of cell units in the V_{act} = 0.4 V activation from the ambient of −20 °C and (b) evolution of total activation current in C-rate during the activation process for selected cases for different thermal conductivities.

voltage varies little due to the small change of SOC; the cell voltage usually increases as can be seen from Fig. 2b; and the internal resistance decreases with increasing temperature. Therefore, the activation current variation depends on the competition between the increasing cell voltage and the decreasing internal resistance. For cell units close to the Ni foil, the rapid temperature rise leads to drastic drop of internal resistance which outweighs the increasing cell voltage, and therefore the activation current greatly increases with time. For cell units far from the Ni foil, the slow temperature increase results in slow drop of internal resistance, and therefore the increasing cell voltage dominates the activation current, making it decrease with time. From the above analysis we can conclude that temperature gradient in the pouch cell is the major reason for the non-uniform current distribution across various cell units.

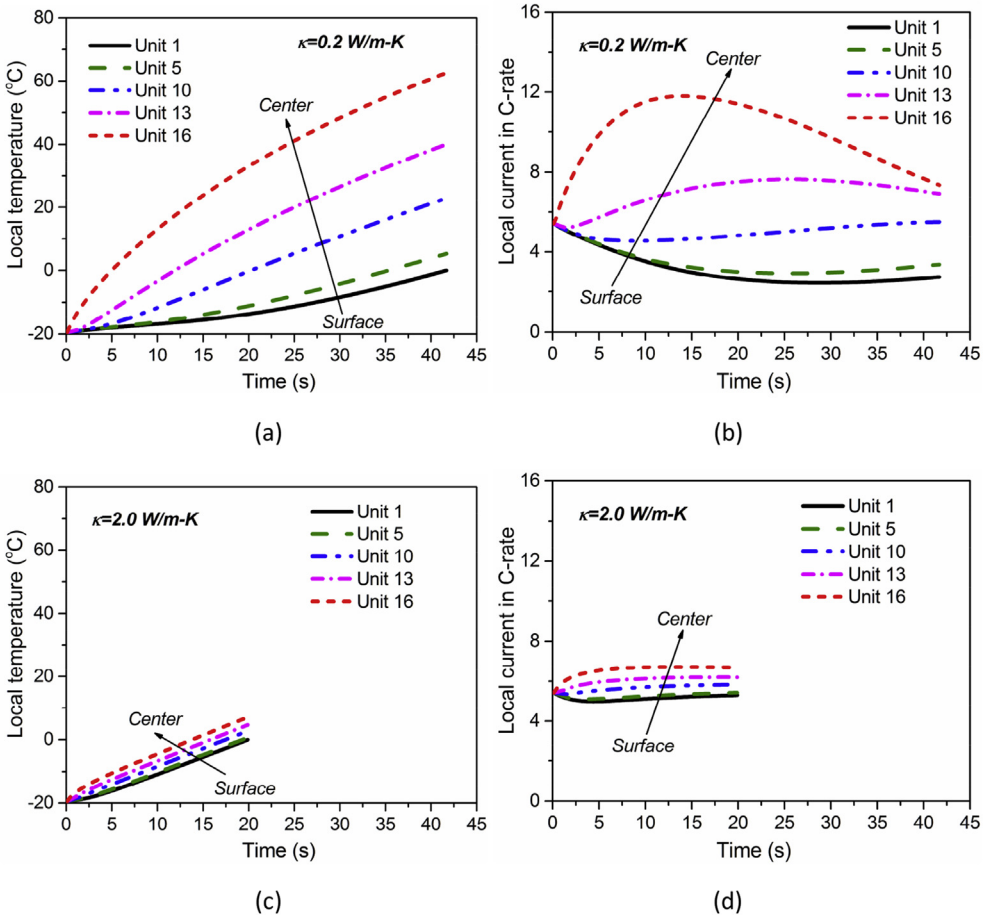

Fig. 6. Variation of local temperature (a&c) and local current in C-rate (b&d) of several selected cell units at different locations of the cell in the V_{act} = 0.4 V activation process from the ambient temperature of −20 °C with different effective thermal conductivity of cell units: (a&b):0.2 W $m^{-1}K^{-1}$; (c&d): 2.0 $m^{-1}K^{-1}$.

It should also be noted that the non-uniform discharge current of different cell units leads to non-uniform SOC among these units, as can be seen from Fig. 4d. The SOC of unit 16 drops by ~6.5% in the activation process due to its high discharge rate, while the SOC of unit 1 drops only ~3.05%. Therefore, during rest or open-circuit period after activation, though the total cell output current is zero, the internal units near to the cell surface continue discharging so as to charge those units in the center, as can be noted from Fig. 4c where positive C-rate indicates discharging and negative C-rate means charging. The maximum charging rate for unit 16, as can be noted from Fig. 4c, is as high as 1.5 C. This internal re-balancing in SOC among various cell units along with thermal gradient relaxation helps to create uniform SOC distribution in practical battery operation.

4.3. Temperature gradient effects on activation time and energy consumption

In this subsection, we numerically explore effects of the temperature gradient on activation time and energy consumption by varying the effective through-plane thermal conductivity of cell units. Fig. 5a displays the Ni foil temperature at the end of activation, the activation time and capacity consumption for cells with different effective thermal conductivities of cell units in the activation from −20 °C to 0 °C. The maximum Ni foil temperature at the end of activation is lowered exponentially with the increasing thermal conductivity, indicating the dramatic easing of temperature gradient with increased thermal conductivity. When the thermal conductivity becomes sufficiently large, the Ni foil temperature approaches the surface temperature (i.e. 0 °C) at the end of activation, implying zero temperature gradient inside the cell. Following the same trend for Ni foil temperature, it is interesting to note that both the activation time and capacity consumption also decrease exponentially and finally stabilize with the increasing cell thermal conductivity. There are two reasons for this beneficial effect. First, the diminishing temperature gradient makes the self-heating process more energy-efficient. Second, the more uniform temperature distribution within the cell boosts the total activation current, as shown in Fig. 5b, which in turn translates to shorter activation time.

Fig. 6 plots the evolution of local temperature and current of several selected cell units in the activation process for a low thermal conductivity case (0.2 W m^{-1} K^{-1}) and a high thermal conductivity case (2.0 W m^{-1} K^{-1}). For the low thermal conductivity case, the temperature gradient is extremely high, with the Ni foil temperature reaching as high as 70 °C after activation, as shown in Fig. 6a. Accordingly, the current distribution becomes much more non-uniform, as shown in Fig. 6b, where the maximum discharge rate of the central cell unit is as high as 12 C. Despite of this high current from the central units, the total activation current of the low conductivity cell, as shown in Fig. 5b, is lower than the high conductivity cell shown in Fig. 6d, indicating that the overall cell performance is limited by inadequate heat transfer in the through-plane direction. When the thermal conductivity is increased to

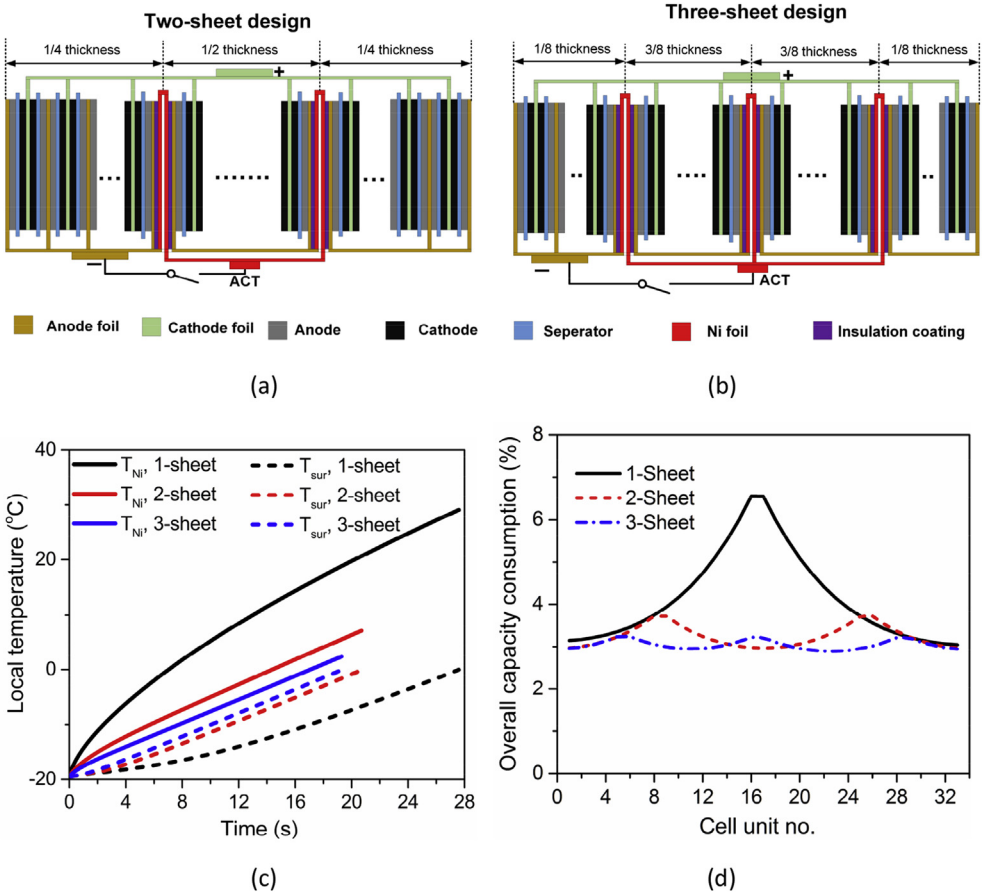

Fig. 7. (a&b): Sketch of multi-sheet designs for self-heating lithium ion battery with reduced temperature gradient, activation time and capacity consumption: (a) two-sheet design (b) three-sheet design. One end of the inserted foils are welded together and connected to the negative (−) terminal; the other end of these foils are welded together and connected to the activation (ACT) terminal. (c&d): Simulation results for cells with the above two-sheet or three-sheet designs in the V_{act} = 0.4 V activation process from the ambient temperature of −20 °C: (c) Variation of surface and nickel foil temperatures (d) Overall capacity consumption of each cell unit with respect to its designed capacity.

2.0 W m^{-1} K^{-1}, both temperature and current distributions become much more uniform, as shown in Fig. 6c and d. The total activation current is also higher.

4.4. Multi-sheet design with more rapid self-heating and less energy consumption

The insight gained above that better heat transfer in the through-plane direction greatly impacts the activation time and energy consumption can be used to discover a major advance in SHLB technology. In this subsection, we computationally create an improved SHLB structure by inserting multiple Ni sheets inside a cell rather than a single sheet in the center. The new design effectively shortens the path of heat transfer from the heat-generating foils to surrounding battery materials and components, potentially substantially improving activation time and energy consumption. Such advanced structures are depicted in Fig. 7a for a 2-sheet design and in Fig. 7b for a 3-sheet design. The multiple Ni sheets are connected in parallel, with one end welded together with the tabs of anode layers and connected to the negative terminal, and the other end welded together and connected to the activation terminal. The overall Ni foil resistance in both advanced designs is kept the same as in the 1-sheet case, i.e. 56.2 mΩ at 20 °C. Thus, the resistance of each sheet at 20 °C in the 2-sheet design is 112.4 mΩ and in 3-sheet design is 168.6 mΩ.

Fig. 7c compares the evolution of surface and Ni foil temperatures in the activation process from ambient of −20 °C for the base case with the two advanced cells. It is noted that the temperature difference between Ni foil and cell surface decreases greatly with the increase of sheet number. Note also that the temperature difference between the foil and outer cell surface, as displayed in Fig. 7c, persists only when the activation current is on. Experimentally it is found that once self-heating is completed or the activation current is off, it usually takes ~5 s for the temperature differences shown in Fig. 7c to fade away, i.e. to re-equilibrate thermally inside the cell. This is to say that thermal and electrical re-balancing among various cell units in a large-format cell is sufficiently fast to be any concern for practical applications. Moreover, the activation time is reduced from 27.7 s for the 1-sheet cell to 20.8 and 19.4 s for the 2-sheet and 3-sheet cells, respectively. These represent 25 and 30% reduction in activation time. Also, the capacity consumption of the activation drops from 4.15% for the 1-sheet cell to 3.23% for the 2-sheet cell and to 3.03% for the 3-sheet cell. These are by 22% and 27% reductions respectively. We further note that the results of the 3-sheet cell are already fairly close to the theoretical limits in activation time (17.5 s) and capacity consumption (2.76%) presented in Fig. 5a for cells with infinitely large thermal conductivity.

Fig. 8 presents the through-plane distributions of temperature and current at different time instants of activation for both 2- and 3-sheet cells. Compared to the 1-sheet cell in Fig. 3, we can see that temperature variations significantly dampen with more pieces of Ni foils inserted, which also proves very beneficial to improved cell durability resulting from thermal cycling. Additionally, the local

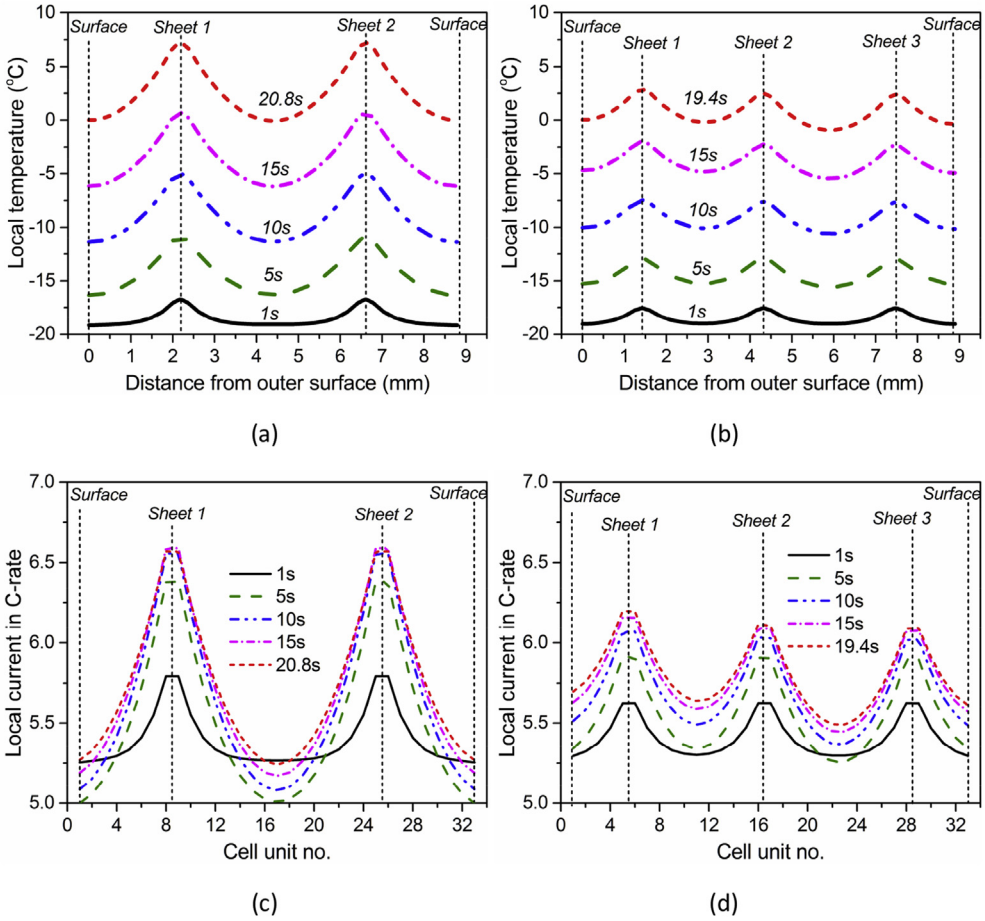

Fig. 8. Distributions of local temperature (a&b) across the cell thickness and local current in C-rate (c&d) of individual cell units at different times of the V_{act} = 0.4 V activation process from the ambient temperature of −20 °C for cells with different designs: (a&c) two-sheet design and (b&d) three-sheet design.

current of cell units near Ni foils decreases while that of cell units far from Ni foils increases with more sheets inserted, leading to much more uniform current distribution. As a consequence, local capacity consumption is more uniform among individual cell units with more Ni foils added, as can be seen from Fig. 7d. This implies that utilization of heating energy is much improved.

As a trade-off between performance boost and simplicity of manufacture, the 2-sheet cell design computationally discovered herein has been transferred to cell builds in our laboratory, and experimental results shall be reported elsewhere [23].

5. Conclusion

We have numerically explored the activation process of the self-heating lithium-ion battery in detail, with the objectives of identifying key factors affecting the self-heating efficiency and optimizing cell designs to achieve more rapid self-heating with less energy consumption. An electrochemical-thermal coupled model has been developed to understand the self-heating battery structure for the first time and to predict the internal characteristics of an SHLB cell. The simulation results reveal the presence of large temperature gradient inside the cell if using a single Ni foil in the middle of the cell. This large temperature gradient results from inadequate through-plane heat transfer and in turn leads to less-efficient heating energy utilization and a highly non-uniform current distribution across the cell thickness. Furthermore, we quantified the impact of the temperature gradient on activation time and energy (capacity) consumption. Finally, we proposed a multi-sheet cell design that is effective in reducing the temperature gradient and feasible as well as easy to implement in practice. Our ECT model forecasted a major advance of 2- and 3-sheet cell designs as compared to the first generation 1-sheet cells, with 25–30% improvement in both activation time and energy consumption as well as enhanced cell durability due to diminishing internal temperature gradient.

Acknowledgements

We thank Drs. Shanhai Ge and Terrence Xu of EC Power for development of the SHLB cells used in this study. We are also grateful to EC Power for offering numerical algorithms and materials database through its AutoLion™ software.

Appendix A. Supplementary data

Supplementary data related to this article can be found at http://dx.doi.org/10.1016/j.jpowsour.2016.08.028.

References

[1] M. Armand, J.M. Tarascon, Nature 451 (2008) 652–657.
[2] V. Etacheri, R. Marom, R. Elazari, G. Salitra, D. Aurbach, Energy & Environ. Sci. 4 (2011) 3243–3262.
[3] C.Y. Wang, G. Zhang, S. Ge, T. Xu, Y. Ji, X.G. Yang, Y. Leng, Nature 529 (2016) 515–518.
[4] Y. Ji, Y.C. Zhang, C.Y. Wang, J. Electrochem. Soc. 160 (2013) A636–A649.
[5] Extreme Temperatures Affect Electric Vehicle Driving Range, AAA Says, http://newsroom.aaa.com/2014/03/extreme-temperatures-affect-electric-vehicle-driving-range-aaa-says/.
[6] C.K. Huang, J.S. Sakamoto, J. Wolfenstine, S. Surampudi, J. Electrochem. Soc. 147 (2000) 2893–2896.
[7] H.P. Lin, D. Chua, M. Salomon, H.C. Shiao, M. Hendrickson, E. Plichta, S. Slane, Electrochem. Solid State Lett. 4 (2001) A71–A73.
[8] S.S. Zhang, K. Xu, T.R. Jow, Electrochim. Acta 48 (2002) 241–246.
[9] S.S. Zhang, K. Xu, T.R. Jow, J. Power Sources 115 (2003) 137–140.
[10] D. Yaakov, Y. Gofer, D. Aurbach, I.C. Halalay, J. Electrochem. Soc. 157 (2010) A1383–A1391.
[11] C.R. Sides, C.R. Martin, Adv. Mater. 17 (2005) 125–128.
[12] C. Li, L. Gu, S. Tsukimoto, P.A. van Aken, J. Mater, Adv. Mater. 22 (2010) 3650–3654.
[13] K. Xu, Chem. Rev. 114 (2014) 11503–11618.
[14] A. Vlahinos, A.A. Pesaran, Energy Efficient Battery Heating in Cold Climates, SAE Technical Paper, 2002. No.2002-01-1975.
[15] T.A. Stuart, A. Hande, J. Power Sources 129 (2004) 368–378.
[16] Y. Ji, C.Y. Wang, Electrochim. Acta 107 (2013) 664–674.
[17] G. Luo, C.Y. Wang, A Multidimensional, electrochemical-thermal coupled lithium-ion battery model, in: Lithium-ion Batteries, CRC Press, 2011, pp. 303–326.
[18] J. Kalupson, G. Luo, C.E. Shaffer, SAE Tech. Pap. (2013) 01–1522.
[19] W.B. Gu, C.Y. Wang, J. Electrochem. Soc. 147 (2000) 2910–2922.
[20] AutoLion™, www.ecpowergroup.com/autolion/, accessed: April 2016.
[21] Y. Leng, C.Y. Wang, unpublished research, University Park, Penn State University Electrochemical Engine Center, 2015. PA 16802.
[22] Y. Ye, L.H. Saw, Y. Shi, K. Somasundaram, A.A.O. Tay, Electrochim. Acta 134 (2014) 327–337.
[23] G. Zhang, S. Ge, T. Xu, X.G. Yang, H. Tian, C.Y. Wang, Rapid Self-heating and Internal Temperature Sensing of Lithium-ion Batteries at Low Temperatures, 2016 submitted for publication.

Nomenclature

c: lithium concentration, mol m^{-3}
c_p: specific heat, J kg^{-1} K^{-1}
D: Diffusion coefficient, m^2 s^{-1}
F: Faraday constant, 96487 C mol^{-1}
I: current, A
j: volumetric current density, A m^{-3}
q: volumetric heat source, W m^{-3}
r: coordinate in the radial direction, m
R: resistance, Ω
t: time, s
t_+: transference number
T: temperature, K
V: voltage, V

Greek

ε: porosity
σ: electronic conductivity, S m^{-1}
κ: electrolyte conductivity, S m^{-1}
κ_D: diffusional conductivity, A m^{-1}
ϕ: electric potential, V
ρ: density, kg m^{-3}
α: temperature coefficient, K^{-1}

Subscripts

act: activation
e: electrolyte phase
s: solid phase
Ni: nickel